Mapana – Journal of Sciences
2025, Vol. 24, No. 3, *45-76*
ISSN 0975-3303 | https://doi.org/10.12723/mjs.74.3

DFT and Molecular Docking Investigations on a Pyrazole Derivative for Antimicrobial Applications

M. Premalatha*, K. Anitha†, B. Revathi‡, V. Balachandran‡, B. Narayana§, A. Jayashree§, T. Raguram**

Abstract

The global surge in multidrug-resistant infections calls for the development of new therapeutic agents. This study presents the preparation and characteristics of a 5-Amino-1-isonicotinoyl-3-(4-nitrophenyl)-2,3-dihydro-1H-pyrazole-4-carbonitrile (AINDPC). Electronic structure and reactivity were evaluated using quantum chemical methods, while molecular docking was used to assess its interaction with microbial target proteins, indicating strong antimicrobial potential. Pharmacokinetic profiling confirmed favorable drug-like characteristics and bioavailability. The compound also exhibited notable antimicrobial activity against various bacterial and fungal strains.

Keywords: Pyrazole derivatives; Antimicrobial activity; Molecular docking; Quantum chemical analysis; Pharmacokinetics.

1. Introduction

The escalating global challenge posed by multidrug-resistant microbial infections has necessitated the development of advanced and innovative research strategies. Conventional strategies that target individual microbial

* Department of Physics, Shrimati Indira Gandhi College, (Affiliated to Bharathidasan University), Tiruchirapalli 620 002, Tamil Nadu, India; prema84sai@gmail.com

† Department of Physics, Government Arts and Science College, (Affiliated to Bharathidasan University), Lalgudi 621712, India; drkanitharesearch@gmail.com

‡ Centre for Research, Department of Physics, Arignar Anna Government Arts College, (Affiliated to Bharathidasan University), Musiri, Tiruchirapalli 621211, India; brevathi1965@gmail.com, brsbala@rediffmail.com

§ Department of Studies in Chemistry, Mangalore University, Mangalagangotri574 199, India; nbadiadka@gmail.com, shree.aj31chem6@gmail.com

** Center for Applied Nanomaterials, Chennai Institute of Technology, Chennai – 600 069, Tamil Nadu, India; raguramt@citchennai.net

agents have become increasingly susceptible to resistance mechanisms, often undermining the long-term efficacy of potential drug candidates [1]. In response, a paradigm shift toward exploring robust and versatile chemical frameworks has gained traction. This challenge has constrained a shift toward innovative approaches, among which pyrazoles, a class of aromatic five-membered heterocyclic compounds, has emerged as a prime focus of intense investigation. Pyrazoles and their derivatives have shown broad utility, particularly in medicinal and agrochemical applications.

Several studies have highlighted the potential of pyrazole-based scaffolds in medicinal chemistry. Adnan A. Bekhit et al. [2] reported the significant anti-inflammatory activity of certain pyrazole derivatives, demonstrating their potential as treatments for chronic inflammatory diseases. Alaa R.I Morsy et al. [3] further expanded the therapeutic scope by evaluating pyrazole derivatives bearing a hydroxyquinoline as antiviral agents, with promising results against emerging viral threats. F.E. Bennani et al. [4] have shown the antitumor effectiveness of these compounds, emphasizing their potential in cancer therapy. This is further supported by their proven effectiveness in combating a range of diseases, indicating their potential for wide-ranging applications. Research by A. Cetin et al. [5] and Ramesh et al. [6] showcases the antimicrobial activity of pyrazole derivatives, underscoring their promise in the fight against drug-resistant pathogens. Their success against resistant microbial strains suggests they may be pivotal in addressing the global issue of antimicrobial resistance. Moreover, Ouyang et al. [7] and Kumar et al. [8] have shown that pyrazole derivatives can also have significant antiviral activity, particularly relevant in the current context of emerging viral diseases, and their anti-inflammatory properties further enhance their relevance in treating chronic inflammatory conditions.

This study aims to explore the biological significance of novel pyrazole derivatives, focusing on their antimicrobial, anticancer, and anti-inflammatory activities. By combining laboratory experiments with in silico approaches, we seek to elucidate the molecular basis of their bioactivity and broaden the therapeutic prospects of pyrazole-based compounds across healthcare domains

A review of the literature reveals that extensive research has been conducted on pyrazole derivatives, serving as a foundation for investigating their spectroscopic and structural characteristics using computational modeling tools. Experimental and theoretical spectral analyses were carried out to investigate the compound's vibrational behavior. Frontier molecular orbital (HOMO–LUMO) analysis provided insights into electron distribution and charge transfer, while global reactivity descriptors and molecular electrostatic potential (MEP) maps helped relate molecular structure to bioactivity. Furthermore, non-covalent interactions and electronic localization were also explored. Molecular docking studies, performed

using protein structures from the Protein Data Bank (PDB), offered a detailed evaluation of the binding affinities and interaction profiles of the most active compound. Unlike previously reported pyrazole derivatives, AINDPC features unique substitutions (isonicotinoyl, 4-nitrophenyl, and cyano groups) that enhance its electronic properties, binding affinity, and pharmacokinetic profile, distinguishing it from known analogues.

2. Materials and methods

2.1. Materials

4-Nitrobenzaldehyde, malononitrile, pyridine, isoniazid, concentrated HCl, ethyl acetate, hexane, and the study utilized double-distilled water. All chemicals were obtained from Sigma and used without further purification.

2.2. Synthesis and characterisation of AINDPC and computational details

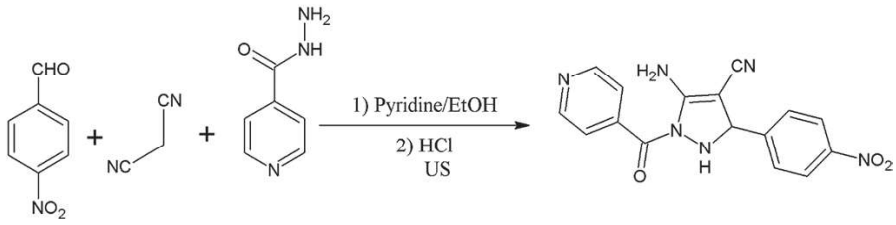

Scheme 1. Synthetic Pathway for 5-Amino-1-isonicotinoyl-3-(4-nitrophenyl)-2,3-dihydro-1H-pyrazole (AINDPC)

Fig. 1 illustrates the preparation, the reaction time, color, and melting point, along with FT-IR, NMR, and elemental analysis of AINDPC provided, which also includes details of the instruments used for the physical characterization. Fig. 2 shows that details of DFT calculations, Multiwfn softwares and molecular docking simulations [9-12].

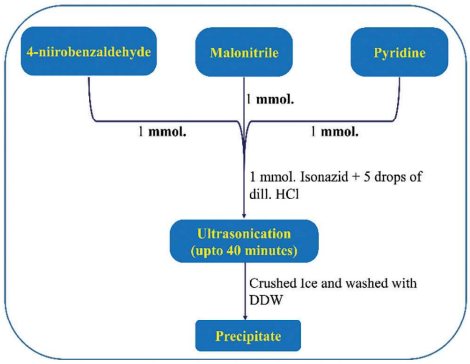

Fig. 1: Synthesis of AINDPC

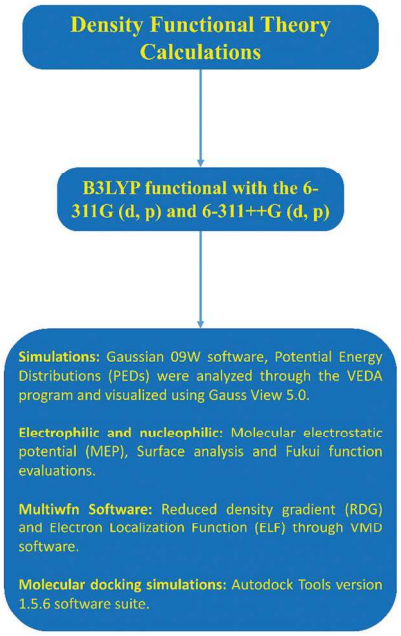

Fig. 2: Computational details, Multiwfn softwares and molecular docking simulations for AINDPC

3. Results and discussion

3.1 Characterization of a new synthesis pyrazole derivative

AINDPC, a newly synthesized organic compound, was obtained with a 74% yield following the procedure outlined in Scheme 1.

Time (min)/Yield (%): 30/74, **Colour:** Orange, **Melting Point (°C):** 256-258

Mass spectrum : Molecular ion peak at **m/z:** 335.95 [M^+-H] in accordance with its molar mass 336.30 (Molecular formula $C_{16}H_{12}N_6O_3$).

Elemental Analysis for $C_{16}H_{12}N_6O_3$ (335.95 g/mol) % : Analytical Calc. C : 57.18; H : 3.64; N : 24.90. Found C : 57.14; H : 3.60; N : 24.99

Its molecular structure was validated by NMR, FT-IR, and elemental analysis. In the FT-IR spectrum, characteristic N-H stretching observed at 3316 and 3300 cm^{-1}. The nitrile (-C≡N) group exhibited a peak at 2220 cm^{-1}, while the carbonyl (C=O) stretching was detected at 1680 cm^{-1}. Additionally, NH bending vibrations were noted at 1586 cm^{-1}. The ^1H NMR spectrum of AINDPC showed a prominent NH proton signal at δ 8.77 ppm, characteristic of the pyrazole ring. Pyridine ring protons (Py-H) generated doublet signals

at δ 8.40 and δ 8.38 ppm. Aromatic ring protons produced signals at δ 8.08 ppm and δ 8.07 ppm. The amino group (-NH_2) proton resonated at δ 7.89 ppm, while the pyrazole ring CH proton appeared at the same chemical shift. In the ^{13}C NMR spectrum, the carbonyl carbon (C=O) was identified by its resonance at δ 164.1 ppm. Furthermore, -C≡N displayed a distinct signal at δ 115.6 ppm. These findings validate the successful synthesis and structural characterization of AINDPC. The carbon in the pyrazole ring displayed their resonance at δ 58.3 ppm. The experimental values obtained through elemental analysis match closely with the values derived from analytical calculations.

3.2. Geometry optimisation

The optimized molecular structure of AINDPC, examined using B3LYP/6-311G++ (d, p) theoretical level, reveals notable relationships between its bond lengths, bond angles, and its biological, electronic, and stability characteristics. Due to the unavailability of crystallographic data for the AINDPC molecule in literature and the calculated structural parameters were evaluated in comparison to those of a similar molecule. [13, 14] outlined in Table 1. Key bond lengths such as N1–N2 (1.45 Å), N1–C5 (1.42 Å), N1–C6 (1.38 Å), and C6–O7 (1.25 Å) longer than reported [16] highlight the influence of delocalized electron density, particularly in regions with resonance and partial double-bond character. Shorter bond lengths, such as N1–C6 and C6 = O7, are indicative of increased electron delocalization, which enhances molecular stability and contributes to its electronic properties, such as lower HOMO-LUMO energy gaps. The optimized structure is shown in Fig. 3. This stability is crucial for maintaining structural integrity during biological interactions. The bond angle deviations of N–N–C from the ideal sp^2 or sp^3 hybridization geometries, reflecting the strain induced by conjugation and electron delocalization. These deviations often enhance molecular reactivity by introducing steric and electronic factors favorable for interactions with biological targets. For example, the angles around the nitrogen centers influence its electrophilicity and nucleophilicity, which are critical for interactions with enzymes or receptors in biological systems. These factors can influence the molecule's ability to align and bind to biological macromolecules, impacting its pharmacological activity.

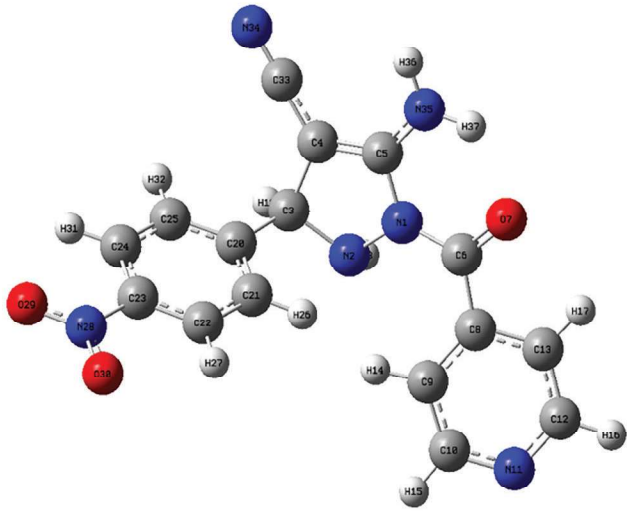

Fig. 3: Optimised geometrical structure of AINDPC

Bond length(Å)			Bond Angle(Å)		
Parameter	B3LYP/ 6311G (d,p)	B3LYP/ 6311G++ (d,p)	Parameter	B3LYP/ 6311G (d,p)	B3LYP/ 6311G++ (d,p)
N1-N2	1.45	1.45	N2-N1-C5	109.18	109.19
N1-C5	1.42	1.42	N2-N1-C6	124.30	124.17
N1-C6	1.38	1.38	C5-N1-C6	126.51	126.62
N2-C3	1.49	1.36	N1-N2-C3	106.46	106.45
N2-H18	1.02	1.04	N1-N2-H18	107.28	107.19
C3-C4	1.53	1.41	C3-N2-H18	110.49	110.14
C3-H19	1.09	2.13	N2-C3-C4	102.56	102.63
C3-C20	1.52	1.51	N2-C3-H19	107.60	107.60
C4-C5	1.37	1.41	N2-C3-C20	113.35	113.39
C4-C33	1.39	1.41	C4-C3-H19	111.58	111.47
C5-N35	1.34	1.34	C4-C3-C20	113.10	113.13
C6-O7	1.26	1.25	H19-C3-C20	108.4 6	108.44
C6-C8	1.49	1.48	C3-C4-C5	109.52	109.69
C8-C9	1.40	1.40	C3-C4-C33	124.92	124.69
C8-C13	1.40	1.41	C5-C4-C33	125.37	125.48
C9-C10	1.40	1.40	N1-C5-C4	109.44	109.46
C9-H14	1.08	1.08	N1-C5-N35	121.00	120.92
C10-N11	1.35	1.35	C4-C5-N35	129.52	129.59
C10-H15	1.08	1.08	N1-C6-O7	118.85	118.83
N11-C12	1.35	1.35	N1-C6-C8	121.82	121.74
C12-C13	1.39	1.39	O7-C6-C8	119.30	119.37
C12-H16	1.08	1.08	C6-C8-C9	126.69	126.43
C13-H17	1.08	1.08	C6-C8-C13	115.39	115.56
C20-C21	1.40	1.54	C9-C8-C13	117.83	117.90

Bond length(Å)			Bond Angle(Å)		
Parameter	B3LYP/ 6311G (d,p)	B3LYP/ 6311G++ (d,p)	Parameter	B3LYP/ 6311G (d,p)	B3LYP/ 6311G++ (d,p)
C20-C25	1.40	1.52	C8-C9-C10	118.72	118.77
C21-C22	1.39	1.36	C8-C9-H14	120.99	120.90
C21-H26	1.08	1.08	C10-C9-H14	120.28	120.31
C22-C23	1.39	1.43	C9-C10-N11	123.57	123.43
C22-H27	1.08	1.08	C9-C10-H15	120.37	120.66
C23-C24	1.39	1.45	N11-C10-H15	116.04	115.90
C23-N28	1.46	1.41	C10-N11-C12	117.44	117.57
C24-C25	1.39	1.35	N11-C12-C13	123.06	122.94
C24-H31	1.08	1.08	N11-C12-H16	116.11	115.96
C25-H32	1.08	1.08	C13-C12-H16	120.81	121.08
N28-O29	1.26	1.29	C8-C13-C12	119.33	119.35
N28-O30	1.28	1.29	C8-C13-H17	119.46	119.46
C33-N34	1.18	1.17	C12-C13-H17	121.19	121.17
N35-H36	1.01	1.01	C3-C20-C21	122.01	121.97
N35-H37	1.01	1.01	C3-C20-C25	118.65	118.77
			C21-C20-C25	119.30	119.22
			C20-C21-C22	120.60	120.64
			C20-C21-H26	119.64	119.73
			C22-C21-H26	119.74	119.62
			C21-C22-C23	118.82	118.88
			C21-C22-H27	121.65	121.63
			C23-C22-H27	119.51	119.47
			C22-C23-C24	121.85	121.75
			C22-C23-N28	119.05	119.09
			C24-C23-N28	119.09	119.14
			C23-C24-C25	118.63	118.69
			C23-C24-H31	119.66	119.63
			C25-C24-H31	121.70	121.67
			C20-C25-C24	120.77	120.79
			C20-C25-H32	119.97	120.02
			C24-C25-H32	119.25	119.17
			C23-N28-O29	118.08	118.19
			C23-N28-O30	118.06	118.16
			O29-N28-O30	123.85	123.64
			C5-N35-H36	119.52	119.65
			C5-N35-H37	118.58	118.82
			H36-N35-H37	121.79	121.44

3.3. Vibrational analysis

Vibrational band modes were computed using the DFT/B3LYP/6-311G++(d,p) level of theory with Gaussian 09 [9]. Molecular structure visualization and validation were performed using GaussView 5.0 [10]. Potential Energy Distribution (PED) analysis was carried out using VEDA 4 software to investigate energy contributions of individual vibrations. For the

AINDPC molecule, which consists of 37 atoms, a total of 105 normal vibrational modes were identified. The vibrational wavenumbers, assignments, and PED contributions are summarized in Table 2, and corresponding spectra are depicted in Fig. 4a and 4b. Experimental wavenumbers were compared with theoretical values, emphasizing detailed assignments of stretching (ν), bending (δ and γ), scissoring (sci), and torsional (τ) motions across various functional groups.

In AINDPC, NH_2 asymmetric and symmetric stretching vibrations appear in the FT-IR spectrum at 3424 and 3316 cm^{-1}, consistent with the expected range for primary amines (3600–3300 cm^{-1}) [15,16]. NH_2 scissoring bands are observed between 1650–1550 cm^{-1}, while out-of-plane wagging modes occur within 900–650 cm^{-1}. Theoretical scissoring and wagging modes are estimated at 1635/1633 cm^{-1} and 726/724 cm^{-1}, respectively. NH_2 twisting modes appear at 306 and 302 cm^{-1} across different basis sets. PED analysis indicates these modes have 99% contribution from symmetric and asymmetric NH_2 stretching, validating the experimental observations.

N–H stretching vibrations typical of heterocyclic structures are observed between 3500–3000 cm^{-1}. Theoretical predictions at 3305 and 3300 cm^{-1} correlate well with the experimental peak at 3300 cm^{-1}, supported by 98% PED contribution. In-plane and out-of-plane N–H bending modes were theoretically estimated at 1585/1581 cm^{-1} and 734/731 cm^{-1}, respectively, showing strong agreement with FT-IR and FT-Raman data.

C–H stretching vibrations associated with the aromatic heterocyclic system were observed between 3100–3010 cm^{-1}. For the pyridine ring, DFT calculations predict stretching vibrations between 3119–2860 cm^{-1} with PED contributions of 97–98%. Corresponding FT-IR peaks were observed at 3115, 3040, and 2925 cm^{-1}, indicating C–H stretching and in-plane bending modes.

In-plane bending aromatic C-H vibrational contributions of 82–67% (PED) were identified in the regions 1600–1400 cm^{-1} and 1290–990 cm^{-1}, often coupled with ring stretching modes. Calculated values using B3LYP/6-311G(d,p) appeared at 1525, 1385, 1378, 1365, 1346, 1335, 1296, 1276, 1238, 1225, and 1070 cm^{-1}, while B3LYP/6-311G++(d,p) produced similar results. Experimentally, a medium-intensity FT-IR peak at 1521 cm^{-1} and a strong Raman peak at 1345 cm^{-1} were observed. Out-of-plane C–H bending vibrations were detected at 1196, 1012, 1006, 993, 975, 948, 930, 890, 855, 784, 748, and 720 cm^{-1}, with PED values ranging from 74% to 62%. A weak FT-IR band at 972 cm^{-1} confirmed these assignments.

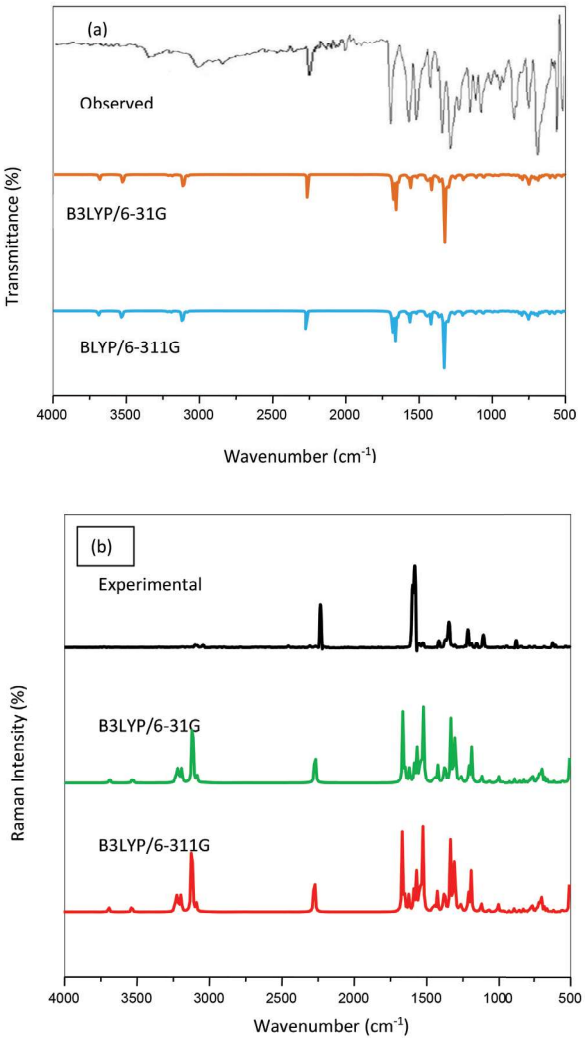

Fig. 4: (a) FT-IR and (b) FT-Raman spectra of AINDPC

The nitrile functional group, characterized by a carbon–nitrogen triple bond, displays a distinct C≡N stretching band typically observed between 2300–2000 cm^{-1}. In the case of AINDPC, this feature appears at 2220 cm^{-1} in the FT-IR spectrum and at 2222 cm^{-1} in the Raman spectrum. C–N stretching vibration, particularly when coupled with NH bending, can be difficult to resolve due to overlap with other modes, yet it generally exhibits moderate to strong intensity in the 1330–1220 cm^{-1} region [17,18]. In this study, the C–N stretching mode is assigned to a band at 1320 cm^{-1}, and at 1309 cm^{-1} in the FT-IR. Corresponding theoretical wavenumbers were predicted at 1313

cm^{-1} and 1310 cm^{-1} using the respective basis sets, further confirming the assignment.

The C=O stretching vibration is easily recognized due to its strong intensity and well-defined appearance within the 1750–1650 cm^{-1} region. This vibrational mode is highly responsive to factors such as ring strain, physical state, and electronic effects from substituents. In this study, the carbonyl group of AINDPC shows a strong absorption at 1680 cm^{-1} in the FT-IR spectrum. This is well supported by theoretical predictions of 1685 cm^{-1} along with a PED contribution of 88%. The location and intensity of ring stretching vibrations are significantly influenced by ring type and substitution pattern. Pyrazole derivatives exhibit distinct C–C ring stretching modes within 1635–1080 cm^{-1}. For AINDPC, aromatic C–C stretching bands are observed in the 1598–1106 cm^{-1} range, consistent with theoretical predictions. A prominent FT-Raman peak at 1596 cm^{-1} supports the presence of ring C–C stretching. The peaks at 1413 and 1212 cm^{-1} in the FT-IR spectrum, along with a Raman peak at 1107 cm^{-1}, further confirm these assignments. These frequencies align with literature values [18,19]. Mixed PED contributions suggest overlapping modes from in- and out-of-plane C–C bending vibrations. Additional calculated modes were observed at 834, 570, 518, 401, and 243 cm^{-1} for the B3LYP/6-311G(d,p) basis set and at 830, 568, 513, 396, and 238 cm^{-1} for B3LYP/6-311G++(d,p). An FT-IR peak at 511 cm^{-1} matches these theoretical values.

In the FT-Raman spectra, the AINDPC molecule exhibits a C-C out-of-plane vibration at 871 cm^{-1}. Theoretical calculations predict this vibration at 875, 565, 375, 230, and 75 cm^{-1} using the In the FT-Raman spectrum, AINDPC exhibits a C–C out-of-plane bending vibration at 871 cm^{-1}. Corresponding theoretical predictions place this vibration at 875, 565, 375, 230, and 75 cm^{-1} (B3LYP/6-311G(d,p)) and at 870, 560, 368, 225, and 78 cm^{-1} (B3LYP/6-311G++(d,p)). Substituents greatly influence both in-plane and out-of-plane ring deformations, typically resulting in bands below 500 cm^{-1}. PED analysis supports the identification of bands at 618 cm^{-1} and 481 cm^{-1} in- and out-of-plane ring vibrations, respectively. Small deviations in wavenumber can be attributed to variations in force constants and mass distribution due to substituent interactions.

The asymmetric stretching vibration of the NO_2 group is generally observed in the 1625–1450 cm^{-1} region, while the symmetric stretch occurs within 1400–1300 cm^{-1}. In the FT-IR spectrum of AINDPC, the asymmetric NO_2 stretch is identified at 1320 cm^{-1}, closely matching a computed value of 1313 cm^{-1} and showing an 88% PED contribution. The symmetric NO_2 stretch appears at 1271 cm^{-1}, with theoretical predictions at 1264 and 1261 cm^{-1} using both basis sets [20,21]. The scissoring, wagging, and rocking modes of the NO_2 group are experimentally observed at 765, 682, and 533

cm^{-1} and theoretically estimated at 763, 680, and 530 cm^{-1}, demonstrating good correspondence between experimental and theoretical data.

Table 2: Vibrational assignments

Mode no	Experimental Wavenumbers (cm^{-1})		Scaled frequencies (cm^{-1})		Vibrational Assignments(PED %)
	FT-IR	FT-Raman	B3LYP / 6311G(d,p)	B3LYP - 6311G++(d,p)	
1	3424		3427	3425	$\upsilon_{ass}NH_2$(99)
2	3316		3318	3315	$\upsilon_{ss}NH_2$(99)
3	3300		3305	3300	υNH(98)
4	3115		3119	3117	υCH(98)
5			3085	3083	υCH(97)
6	3040		3046	3042	υCH(98)
7			3012	3011	υCH(98)
8			2975	2971	υCH(98)
9	2925		2930	2926	υCH(97)
10			2905	2903	υCH(98)
11			2875	2871	υCH(98)
12	2855		2860	2858	υCH(98)
13	2220	2222	2234	2230	υCN(97)
14	1680		1685	1682	υCO(88)
15			1635	1633	$\delta_{siccsoring}NH_2$(80)
16		1596	1598	1595	υCC(81); CH(16)
17	1586	1581	1585	1581	δNH(76)
18		1560	1560	1561	υCC(79)
19	1521	1525	1525	1523	δCH(80)
20			1506	1502	υCC(75); δCH(16)
21			1485	1480	υCC(72); δCH(17)
22		1480	1444	1442	CH (72); δCH(17)
23	1413	1415	1416	1413	υCC(82); δCH(14)
24			1406	1401	υCC(78); δCH(16); δCN(10)
25			1385	1382	δCH(82)
26			1378	1375	δCH(80)
27			1365	1360	δCH(82)
28	1346	1345	1346	1345	δCH(82)
29			1335	1331	δCH(82)
30	1320		1326	1322	$\upsilon_{ass}NO_2$(88)
31	1309		1313	1310	υCN(74); δCH(14), δCO(12)
32			1296	1292	δCH(82)
33			1276	1275	δCH(82)

Mode no	Experimental Wavenumbers (cm^{-1})		Scaled frequencies (cm^{-1})		Vibrational Assignments(PED %)
	FT-IR	FT-Raman	B3LYP / 6311G(d,p)	B3LYP - 6311G++(d,p)	
34			1264	1261	$\upsilon_{ss}NO_2$(84)
35			1238	1233	δCH(75)
36			1225	1220	δCH(74)
37	1212	1214	1216	1213	υCC(76)
38		1194	1196	1195	γCH(72)
39			1182	1180	δCH(78)
40			1166	1163	υNN(74)
41	1153	1154	1155	1153	υCC(75)
42	1113		1116	1115	υCC(72), δCH(78)
43		1107	1110	1106	δCH(74)
44			1092	1091	υCCl(69);υCC(16); δCH(12)
45		993	1070	1067	δCH(67)
46			1041	1038	δ_{ring}(68)
47	1009		1012	1010	γCH(62)
48			1006	1001	γCH(62)
49			993	989	γCH(62)
50			980	978	δ_{ring}(60)
51	972		975	970	γCH(64)
52			948	943	γCH(64)
53			930	927	γCH(63)
54	935		905	901	δCO(74)
55			890	888	γCH(64)
56		871	875	870	γCC(60)
57	850		855	852	γCH(74)
58			834	830	δCC(68), δCH(12)
59			800	798	δ_{ring}(61)
60	779		784	780	γCH(69)
61			765	763	$\delta_{sciss}NO_2$(73)
62	746		748	745	γCH(68)
63			734	731	γNH(67)
64			726	724	$\gamma_{wagging}NH_2$(73)
65			720	716	γCH(65)
66			710	707	δ_{ring}(68)
67			696	695	γCO(65)
68	682		683	680	$\sigma_{wagging}NO_2$(63)
69			670	667	δNH(67)
70			645	643	δ_{ring}(65)
71	618	622	625	620	δ_{ring}(64)

Mode no	Experimental Wavenumbers (cm^{-1})		Scaled frequencies (cm^{-1})		Vibrational Assignments(PED %)
	FT-IR	FT-Raman	B3LYP / 6311G(d,p)	B3LYP - 6311G++(d,p)	
72			610	607	δ_{ring}(64)
73			600	593	γCH(65)
74			579	575	δ_{ring}(70)
75			570	568	δCC(62), δCN(10)
76			565	560	γCC(58)
77			547	542	δ_{ring}(60)
78	530		533	530	$\delta_{rocking}NO_2$(66)
79	511		518	513	δCC(64)
80	481		484	480	γ_{ring}(58)
81			463	459	γ_{ring}(58)
82			437	433	γ_{ring}(55)
83	422		422	420	δCO(66)
84			401	396	δCC(63)
85			382	379	γCO(62)
86			375	368	γCC(68)
87			350	345	δCN(66)
88			306	302	τNH_2(56)
89			282	277	δ_{ring}(75)
90			257	251	δ_{ring}(70)
91			243	238	δCC(68)
93			230	225	γCC(62)
93			221	217	δ_{ring}(60)
94			207	201	γCN(56)
95			178	174	γ_{ring}(52)
96			146	139	δ_{ring}(60)
97			108	105	τNO_2(53)
98			102	97	γCN(56)
99			93	89	δCN(69)
100			78	75	γCC(58)
101			73	69	γ_{ring}(56)
102			55	52	γ_{ring}(54)
103			49	45	γ_{ring}(50)
104			28	31	γ_{ring}(49)
105			22	20	γ_{ring}(49)

υ; Stretching, $\upsilon_{ass;}$ asymmetric Stretching, $\upsilon_{ss;}$ symmetric Stretching δ; in-plane bending, γ; out-of-plane bending, τ; torsion.

3.4. Surface analysis of molecular electrostatic potential

One of the most crucial methods for illuminating the molecular charge distribution on substances is the molecular electrostatic potential (MEP) approach. Compounds' chemical and biological reactivity can be examined using MEP [21]. The MEP technique has been used to analyze charge distribution on AINDPC. Fig. 5 illustrates how different colors correspond to different kinds of potential. The most negative potential zone is represented by the color red, whereas the greatest positive potential region is represented by the color blue [22]. The highest negative potential areas, with values of -0.268, -0.266, -0.447, -0.094, and -0.837, -0.320 a.u., respectively, were found primarily around the O30, O29, O7, N34, and N35, N11 atoms. The findings indicate that the nitrogen atoms at both compound sites have potential values that are near to one another. This could be explained by the fact that the same groups are present on both sides of the molecule's central pyrazole ring. With values of 0.184, 0.203, 0.202, 0.170, 0.354, and 0.388 a.u., respectively, the most favorable potential areas for the AINDPC molecule were found to be around the H16, H17, H19, H20, H36, and H37 atoms.

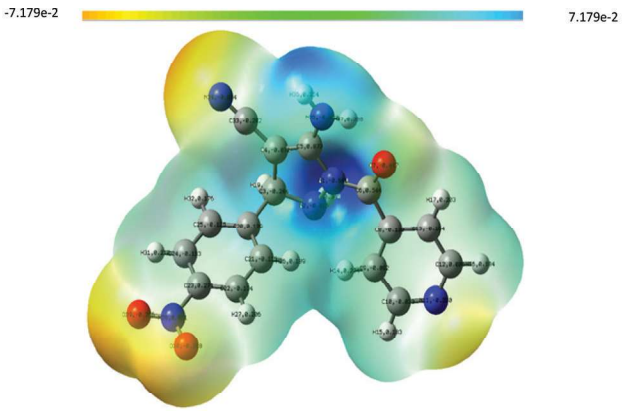

Fig. 5: Molecular electrostatic potential surface of AINDPC

3.5 FMO analysis

The FMO analysis of AINDPC highlights its potential pharmacological properties, supported by detailed electronic parameter calculations. The HOMO energy (-5.3026 eV) indicates high nucleophilicity and potential as an electron donor, often associated with antimicrobial and antioxidant activity, while the LUMO energy (-3.6147 eV) reflects high electrophilicity and potential as an electron acceptor, suggesting anticancer and anti-inflammatory properties. The moderate HOMO-LUMO energy gap (ΔE = 1.6879 eV) implies balanced photoreactivity, favoring electronic transitions. Ionization potential (I = 5.3026 eV) and electron affinity (A = 3.6147 eV) indicate a greater likelihood of losing electrons than gaining them, suggesting

AINDPC's involvement in oxidation reactions [1]. High electronegativity (χ = 4.4586 eV) further supports potential antioxidant activity, while the chemical hardness (η = -0.8439 eV) and softness (S = -1.1849 eV) values reveal a balance between stability and reactivity. This balance is crucial for maintaining the compound's structural integrity during biological interactions. The electrophilicity index (ω = -8.3885 eV) and nucleophilicity index (N = -0.1192 eV) suggest that AINDPC can effectively participate in reactions with electrophiles and nucleophiles, enhancing its adaptability in biological systems shown in Table 3 and Fig. 6**.** AINDPC's enhanced reactivity and greater stability, attributed to its lower chemical softness and smaller band gap. A smaller band gap implies enhanced reactivity, which could lead to more diverse and potentially beneficial interactions with biological systems. These calculated properties suggest that AINDPC combines chemical stability with the ability to interact dynamically within biological environments, making it a strong candidate for applications in drug development and the design of functional materials.

Table 3: AINDPC FMOs and other molecular property values

Parameters	B3LYP/6-311G(d,p) (eV)
ELUMO	− 3.6147
EHUMO	− 5.3026
ΔE (ELUMO - EHOMO)	1.6879

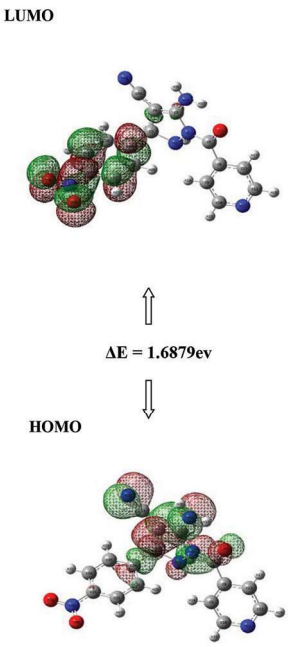

Fig. 6: Frontier molecular orbital of AINDPC

3.6. NMR Spectral interpretation

The structural elucidation of the synthesized compound was established by both ^{1}H and ^{13}C NMR spectral data. The ^{1}H NMR spectrum (δ, ppm) revealed a singlet at δ 8.77 ppm, associated to the –NH proton. Two sets of doublets at δ 8.40 and 8.38 ppm (J = 4.4 Hz, 2H each) corresponding to the aromatic protons of the pyridine ring (Py-H). Similarly, doublets at δ 8.08 and 8.07 ppm (J = 6.8 Hz, 2H each) are assigned to the protons on the substituted phenyl ring (Ar-H). A singlet at δ 7.89 ppm integrating for two protons is consistent with the $–NH_2$ group, while a singlet at δ 7.59 ppm is attributed to the proton (–CH) adjacent to the pyrazole core.

The ^{13}C NMR spectrum further confirmed the structural framework. The signal at δ 164.4 ppm corresponds to the carbonyl (C=O) carbon. Resonances at δ 150.8, 148.5, 146.9, and 140.7 ppm are attributed to aromatic and heteroaromatic carbons. Peaks at δ 129.3, 128.6, and 124.5 ppm represent additional aromatic carbons, while the nitrile carbon (–C≡N) appears at δ 115.6 ppm. The (–CH) of the pyrazole ring is observed at δ 58.3 ppm. These assignments are consistent with the proposed structure and are illustrated in Fig. 7a and 7b.

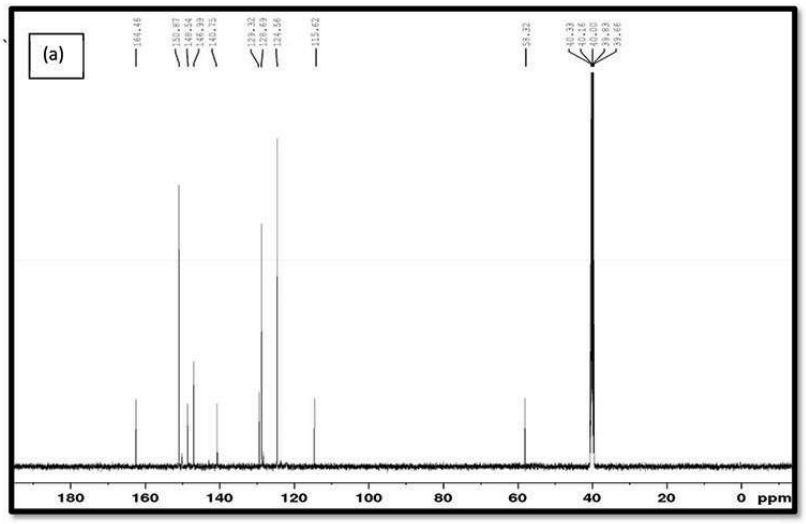

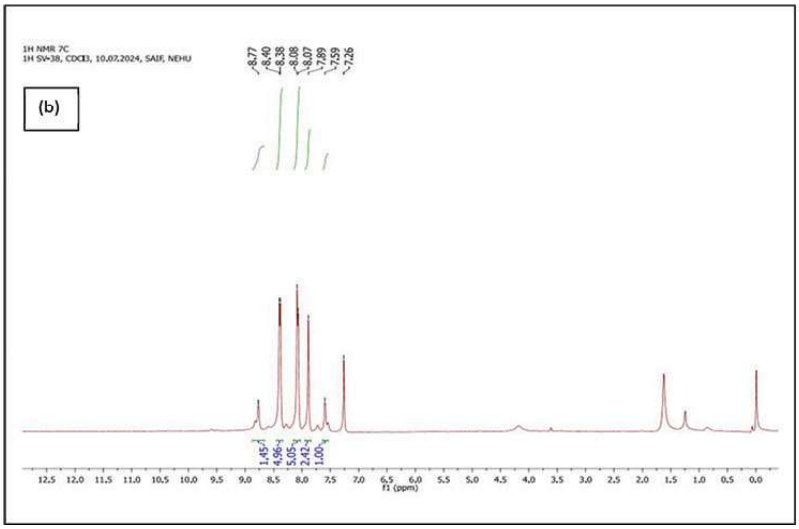

Fig. 7: (a) 13C NMR and (b) ^{1}H NMR spectra of AINDPC

3.7. Non-Covalent interactions

The reduced density gradient (RDG) method offers a graphical representation of various non-covalent interactions (NCI) within a molecule by mapping them in real space. In the corresponding RDG scatter plot, RDG values are plotted against sign(λ_2)ρ, where λ_2 is the second eigenvalue of the Hessian matrix of electron density. This metric efficiently differentiates interaction types: a negative $\lambda_2(\rho)$ value indicates attractive forces such as hydrogen bonding, whereas a positive $\lambda_2(\rho)$ signifies repulsive forces, typically associated with steric hindrance.

Fig. 8a displays the 2D RDG scatter plot and the corresponding isosurface for the title compound . Blue regions on the isosurface represent strong attractive interactions, steric repulsion indicated by red, and weak van der Waals interactions are shown by green. Similarly, Fig. 8b shows the RDG isosurface and scatter plot for another conformation, reflecting similar interaction patterns. A pronounced peak near −0.025 a.u. in the scatter plot confirms the presence of significant hydrogen bonding interactions. The blue-colored zones in the isosurface further highlight these interactions, especially between C–H and oxygen atoms. Red regions, mainly localized in the core regions of the pyrazole, pyridine, and carbonitrile groups, denote areas of strong steric repulsion. Additionally, green regions attributed to H–H interactions reveal van der Waals forces contributing to the molecular packing and stability.

3.7.1. Study of electron localization and orbital confinement

Surface analysis of covalent bonds involves using electron density localization and orbital mapping to generate maps that identify regions with a high probability of electron pair localization. Fig. 8 c and 8d presents the electron density charge distribution in the form of ELF and LOL color maps. The ELF values range from 0.00 to 1.0, where values between 0.5 and 1.0 indicate the presence of localized bound or unbound electrons, while values below 0.5 signify the existence of delocalized electrons. The red-colored areas display the highest concentration of localized electrons. All atoms of nitrogen, oxygen and hydrogen demonstrate localized electron behavior. The electron distribution occurs within the bond areas between the rings of pyrazole and pyridine. Each C and N atom displays a blue electron cloud that extends from them in the molecular structure. The atoms or other molecules from these locations will establish interactions with this molecule. The LOL analysis reveals the presence of delocalized electrons distributed across all C, O, and N atoms, while localized electrons are observed between H atoms and within the interatomic bond regions of the pyrazole and pyridine rings. The molecular electrostatic potential (MEP) surface map further indicates that the O7, O29, and O30 atoms exhibit slightly electron-rich characteristics, whereas the N11, N34, and N35 atoms display pronounced electrophilic properties. The title molecule's electrophilic and nucleophilic regions became visible through ELF and LOL and MEP map analysis which showed good agreement.

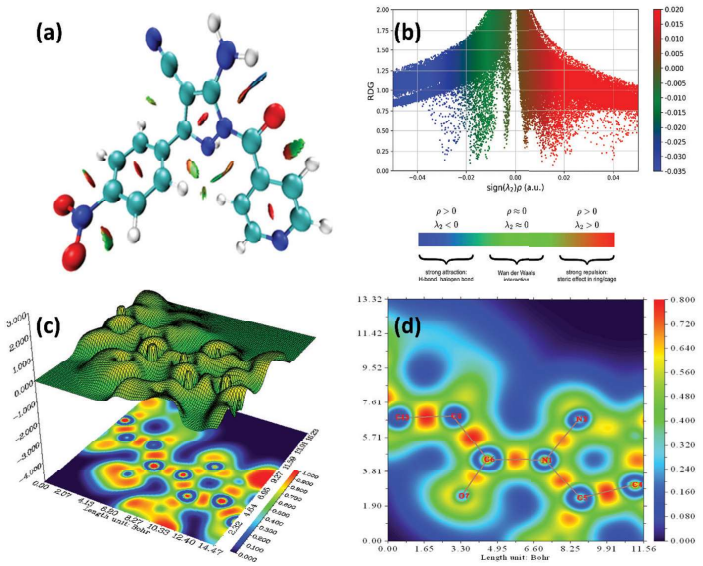

Fig. 8: (a) RDG, (b) RDG Vs λ(2)ρ, (c) ELF color-filled map and (d) LOL color-filled map of AINDPC

3.8. BOILED-Egg Model:

The BOILED-Egg model was utilized to predict the permeability of the blood-brain barrier (BBB) and gastrointestinal (GI) absorption. The development of CNS drugs faces significant challenges because the BBB restricts entry of biological molecules of neurotherapeutics for treating brain disorders. The blood-brain barrier blocks 98% of all tiny compounds from entering the brain. The evaluation of BBB transition activity should be an early priority during drug design for CNS illnesses. The extent to which medication candidates are absorbed through the intestinal system determines their oral bioavailability. The study of GI absorption for these compounds represents a necessary step. PGP functions as an ATP-binding cassette (ABC) transporter. The biological barrier performs two essential functions by removing toxic substances and foreign substances from cells while facilitating drug absorption and extraction. The excessive expression of ABC transporters results in multidrug resistance (MDR), significantly contributing to treatment failure in various diseases, especially cancer. The BOILED-Egg approach utilizes compound SMILE strings to determine human gastrointestinal absorption and blood-brain barrier penetration. The algorithm employs two physicochemical properties including polarity (TPSA) and lipophilicity (WLOGP). Model Fig. 9 shows a substance with high penetration and absorption properties throughout the GI tract and BBB which results in a yellow zone. The chemicals in the whitish region show weak penetration through the blood-brain barrier but strong absorption through the gastrointestinal tract. The chemical shows potential for PGP-mediated efflux from the Central Nervous System (CNS) based on the blue (+) and red (-) dots. The red dot position of our compound indicates positive GI absorption and negative BBB penetration and negative PGP effect on the molecule. TPSA stands as the main factor responsible for the negative BBB outcome. Our compound has a Total Polar Surface Area (TPSA) of 138.18 $Å^2$ below 140 $Å^2$, which suggests good drug transport properties through cell membranes.

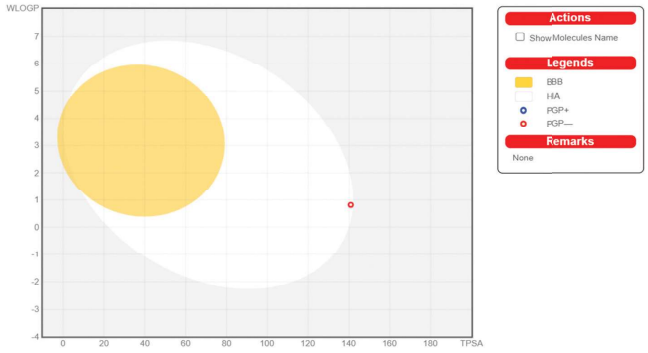

Fig. 9: BOILED-Egg model of AINDPC

3.9. Interpretation of Antimicrobial Activity

The antibacterial potential of the AINDPC compound was evaluated using the agar well diffusion method, which allows the test compound to diffuse through the agar medium and inhibit microbial growth. The study focused on two bacterial strains: *Staphylococcus aureus*, a Gram-positive pathogen commonly associated with bloodstream infections, pneumonia, and osteoarticular diseases; and *Escherichia coli*, a Gram-negative bacterium frequently linked to urinary tract infections, pneumonia, and meningitis. After a 24-hour incubation period, the diameters of the inhibition zones were measured and recorded.

Fig. 10 illustrates the antibacterial effect of AINDPC on the tested pathogens. As shown in Table 4, the compound 5-Amino-1-isonicotinoyl-3-(4-nitrophenyl)-2,3-dihydro-1H-pyrazole-4-carbonitrile demonstrated concentration-dependent activity against *Staphylococcus aureus*, indicating moderate antibacterial efficacy [22, 23]. The nature and position of substituents on the pyrazole ring significantly influenced its antibacterial profile. Structure–Activity Relationship (SAR) analysis suggests that structural variations within the molecule are closely associated with its bioactivity. AINDPC exhibited strong antibacterial activity against *Staphylococcus aureus* and moderate effectiveness against *E. coli*, highlighting its promising potential, particularly against Gram-positive bacterial strains.

Table 4: Antimicrobial activity of 5-Amino-1-isonicotinoyl-3-(4-nitrophenyl)-2,3-dihydro-1H-pyrazole-4-carbonitrile

Microbial strains	DMSO Extract 100 ml added and Zone of inhibition (mm)				
	25 mg	50 mg	75 mg	100 mg	Control
Staphylococcus Aureus	NA	NA	NA	22	24
E. coli	NA	NA	6	10	18

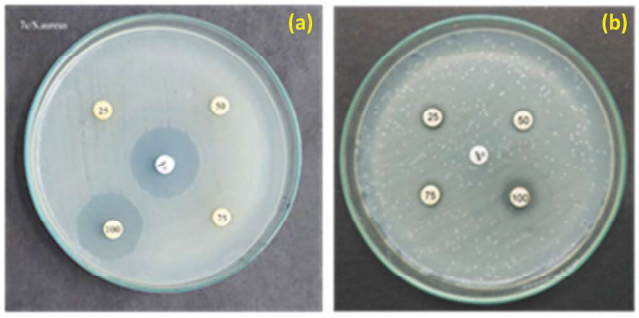

Fig. 10: Antimicrobial activity test for AINDPC compound in (a) S. Aureus and (b) E. Coli

4. Molecular docking

Molecular docking methods predict molecular interactions while calculating the energy levels between interacting molecules. The method establishes the best position for the ligand to face the molecule under investigation. The active protein cavity contains the small molecule ligand. Molecular docking studies enable researchers to predict binding modes and functional group proximity [24, 25]. The Autodock tool [13] enabled researchers to perform molecular docking simulations of AINDPC to investigate potential binding interactions between the synthesized molecule and PDB IDs 4URM, 6EZQ, 5U3A and 2I3B. A molecular docking analysis was conducted to understand better the binding interactions of the most active analogues [26]. Molecular docking represents an effective computer program which helps researchers study binding mechanisms. The web-based prediction tool PASS [27] enables users to forecast various types of activities. The Protein Data Bank (PDB) served as the source for protein collection. The local search system and LGA execute docking stimulations. The software correctly determined all aspects of ligand molecule orientation together with torsion and initial position. The Kollman unified atom type charges and the redemption parameter were employed to generate affinity grid maps through the Autogrid application with 126×126×126 grid points. Calculations of Van der Waals and electrostatic terms were performed using AutoDock parameters with a distance-dependent dielectric model [28, 29]. The PDBQT format saved both protein and ligand molecules before Autodock performed the docking process. **Fig. 11 (a-d)** displays the Poseview diagrams for the AINDPC interaction with the protein. The Ramachandran plot (Fig. 12) was utilized to analyze the stereochemical quality of the protein.To find the proteins with the best fit interactions and the lowest binding energy value, several docking runs have been carried out. Ligand molecule AINDPC produced Pi-Alkyl, Pi-Anion, Conventional hydrogen link, Amide-Pi, Carbon hydrogen bond, and Pi-Pi T-shaped complexes with 4URM, 6EZQ, 5U3A and 2I3B target proteins.

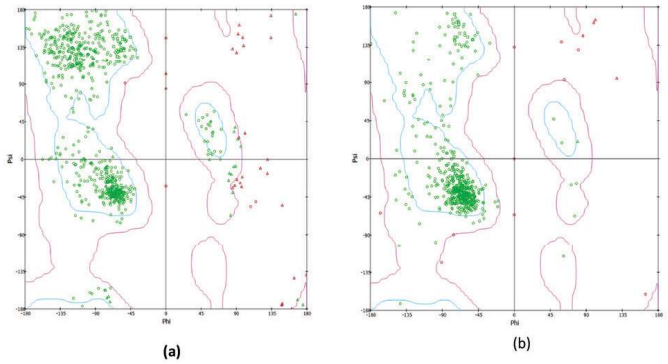

(a) (b)

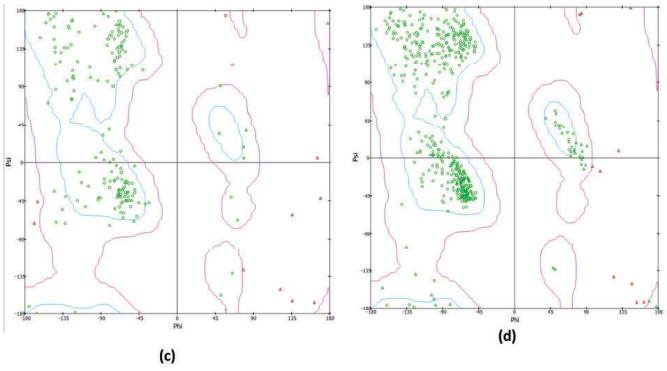

Fig. 12: Ramachandran plot of (a) 4URM, (b) 6EZQ, (c) 2I3B, (d) 5U3A to assess the quality of the protein.

4.1. Docking of AINDPC with protein (PDB ID: 4URM)

The newly synthesized AINDPC shows significant interactions with amino acid residues like ARG B:144; ARG B:84; GLY B:85; GLU B:58; GLY B:83; ILE B:86; PRO B:87; TYR A:138; GLY A:189; LYS A:190; HIS A:146; LEU A:115; ILE A:115; ARG A:186 in AINDPC as illustrated in Table5 and **Fig.11 a**. The compound AINDPC with 4URM exhibits three hydrogen bonding (ARG B:144; ARG B:84 and GLY B:85) and one pi-Anion (GLU B:58) with one pi-Alkyl (ILE B:86) and one carbon hydrogen bond (GLY B:83) interactions. The conventional hydrogen bond lengths are 5.68, 3.54 and 3.75 (between NO_2 and C ≡ N atom) of AINDPC.

4.2. Docking of AINDPC with protein HSA (PDB ID: 6EZQ)

AINDPC appears to be bound to the active sites of the amino acids, With 6EZQ exhibits three hydrogen bonding (TYR A:138; GLY A:189 and LYS A:190), with one Pi-Cation (HIS A:146) and three Pi-Alkyl (LEU A:115; ILE A:115 and ARG A:186). The conventional hydrogen bond lengths are 4.90, 2.83 and 5.15 (between NH_2, C ≡ N and O29 atom) of AINDPC (**Fig.11 b)**.

4.3. Docking of AINDPC with protein (PDB ID: 5U3A)

The molecular docking shows, ALA A:224; ASN A:216; TYR A:2, GLYA:225, LYS A:227, SER A:3 of (PDB ID: 5U3A), are found to interact with AINDPC. With 5U3A has three hydrogen bonding (ALA A:224; ASN A:216; TYR A:2) and one Pi-lone pair (GLYA:225). The conventional hydrogen bond lengths are 2.17, 2.19 and 1.70 (between N35, N34 and O29 atom) of AINDPC (**Fig.11 c)**.

4.4. Docking of AINDPC with protein (PDB ID: 2I3B)

AINDPC binds at the active sites of ARG A:107, ASP A:33; ASN A:97 and LYS A:26 with a bond distance of 5.84, 3.73, 3.73 and 5.14 Å forms hydrogen

bonding with 2I3B. The conventional hydrogen bond lengths are 3.73, 5.84, 3.73 and 5.14 (between NH_2, NO_2, C=O and N11 atom) of AINDPC (**Fig.11 d)**.

AINDPC exhibits significant hydrogen bonding interactions (green), accompanied by notable interactions such as carbon-hydrogen bonds (light green), pi-sigma interactions, pi-alkyl interactions, and pi-cation/anion interactions. The lowest binding energy value demonstrated the bioactive nature of the chemical. Table 5 lists the binding energies (kcal/mol) and inhibition constants (µm) obtained from molecular docking. An important factor in a drug's affinity for attaching to receptors is its hydrogen bonding. A high capacity for binding between a ligand and a protein is demonstrated by a strong hydrogen bonding relationship. Hydrogen bonds typically form between an electronegative atom (such as nitrogen or oxygen). The oxygen atoms of the nitro group and the nitrogen of carbonitryl are the sole locations that are undergoing hydrogen bond formation, according to the ligand interactions with the proteins. The fact, bond lengths of N28-O29 (1.26 Å) and N29-O30 (1.28 Å) are longer than the typical N-O (1.20 Å) bond length validates that the oxygen atom in the amide group and the nitrogen in the carbonitryl group are the sites for hydrogen bond formation. The docked ligand establishes stable complexes with the receptors, yielding minimum binding affinity values of -4.30 kcal/mol for protein 4URM, -6.49 kcal/mol for protein 6EZQ, -10.09 kcal/mol for protein 5U3A, and -6.76 kcal/mol for protein 2I3B. 5U3A shows the least energy of binding at −10.09 kcal/mol.

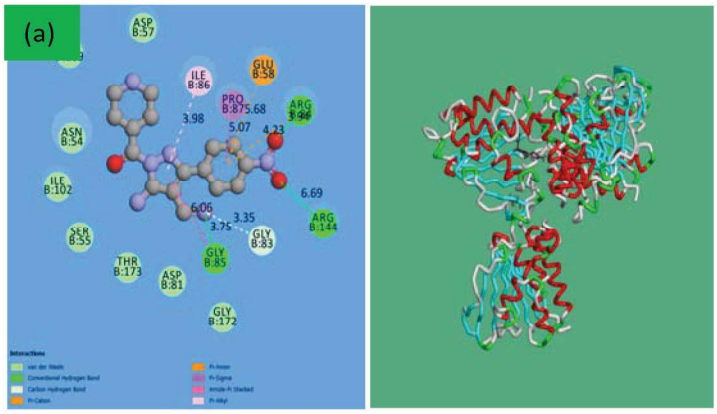

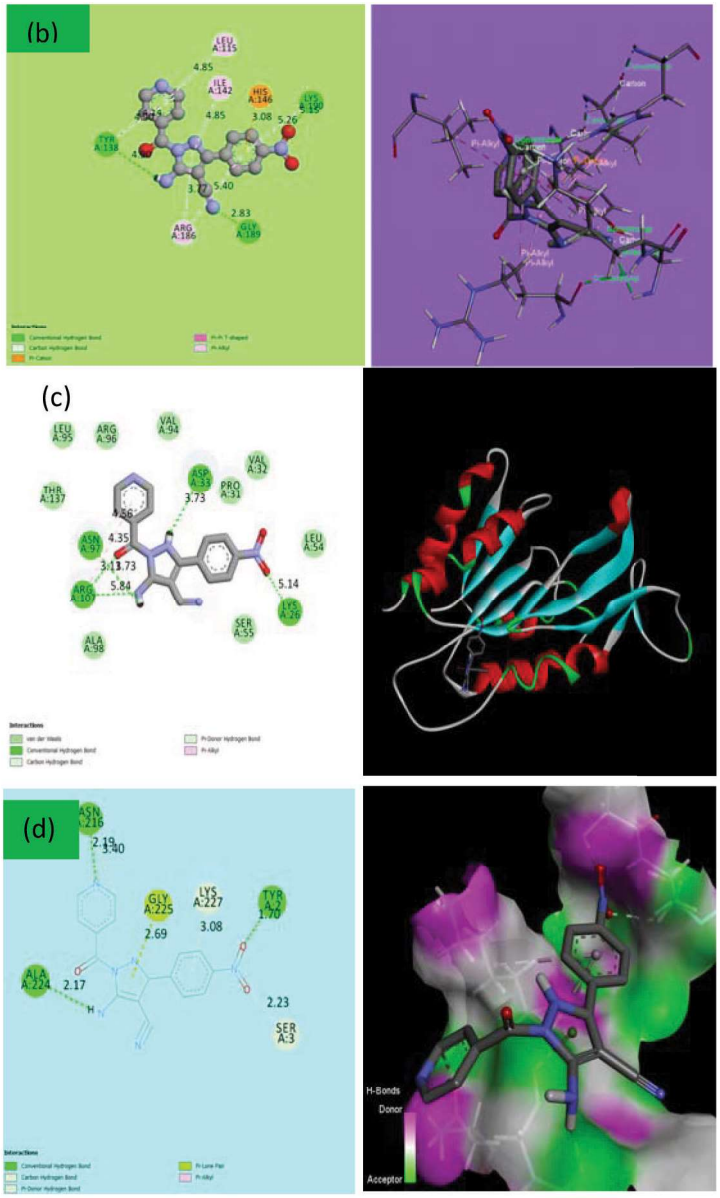

Fig.11: Schematic diagram for the docked confirmation of the active site of the AINDPC compound with (a) 4URM, (b) 6EZQ, (c) 2I3B, (d) 5U3A.

Table 5: Bonded residues, number of hydrogen bonds, bond distance, binding energy and Inhibition constant of AINDPC.

Protein (pdb code)	Bonded residues	hydrogen bonds	Bond distance	Binding energy (kcal/mol)	Inhibition constant
4URM	ARG B:144	3	5.68	-4.30	70.14 µm
	ARG B:84		3.54		
	GLY B:85		6.69		
	GLU B:58		3.75		
	GLY B:83		3.35		
	ILE B:86		3.98		
	PRO B:87		5.07		
6EZQ	TYR A:138	3	4.90	-6.49	17.59 µm
	GLY A:189		2.83		
	LYS A:190		5.15		
	HIS A:146		3.08		
	LEU A:115		4.85		
	ILE A:115		4.85		
	ARG A:186		3.77		
5U3A	ALA A:224	3	2.17	-10.09	39.99 µm
	ASN A:216		2.19		
	GLY A:225		2.69		
	LYS A:227		3.08		
	TYR A:2		1.70		
	SER A:3		2.23		
2I3B	ASP A:33	4	3.73	-6.76	11.14 µm
	ARG A:107		5.84		
	ASN A:97		3.73		
	LYS A:26		5.14		

5. Druglikeness properties

The process of developing new drugs is a lengthy one, fraught with high risk, high investment, and a very high attrition rate. A significant attrition rate of roughly 93% is faced by the preclinical stage, which establishes the essential foundation and is a challenging step in drug development [30]. It is anticipated that over 75% of drug candidates will not succeed during phase I, II, or III clinical trials, as well as in the later stages of the drug approval process, despite some advancing to clinical evaluations. About 40% of candidate molecules fail in this procedure because of undesirable pharmacokinetic characteristics, such as absorption, distribution, metabolism, and excretion (ADME) qualities. Toxicology, a key assessment criterion in drug development, accounts for nearly 30% of the failures encountered during the process. This emphasizes how ADME and toxicity (ADMET) features have a significant influence on whether drug development efforts

are successful overall and how crucial it is to evaluate ADMET properties early on. The 119 ADMET endpoints in ADMET 3.0 are made up of 36 toxicity properties, 8 toxicophore rules, 9 absorption, 9 distributions, 14 metabolisms, 2 excretions, 21 physicochemical, and 20 medical chemistry in **Fig. 13 and 14.** As per Lipinski's Rule of Five, ligand molecules intended for oral administration should comply with at least four out of the five criteria, allowing no more than one violation. The molecular weight of the drug molecule must be 500 Da or less, and its partition coefficient (Log P) should not exceed one, its hydrogen bond donor value cannot exceed five, its hydrogen bond acceptor value cannot exceed ten, and it can violate the rule no more than once. The anticipated toxicity, adsorption, distribution, metabolism, excretion, and physiochemical effects are listed in Table 6 and 7. The absorption of a drug by the body is significantly influenced by its physicochemical properties, particularly its molecular weight (MW) and surface area [24]. For the compound AINDPC, the molecular weight is 336.1 Da. Surface area plays a crucial role in predicting drug distribution, which depends on the number of rotatable bonds and the total count of polar atoms such as hydrogen, nitrogen, and oxygen. These parameters suggest that AINDPC may have low oral bioavailability. Rotatable bonds enhance the flexibility of the therapeutic molecule, aiding its interaction with the binding sites of target proteins [31]. AINDPC contains four rotatable bonds, and its surface area of 138.18 Å² further supports the indication of limited oral bioavailability. There have been two infractions of Lipinski's rule for AINDPC in total. However, only oral medications will be subject to these regulations. With a rate of -4.911, AINDPC shows intestinal absorption and Caco-2 permeability. Skin permeability rate is 0.844 for AINDPC. The blood-brain barrier (BBB) serves as a protective filter, preventing harmful substances from entering the brain and thereby reducing toxicity, side effects, and unintended neurological activity. AINDPC exhibits a blood-brain permeability value of 0.17, confirming that it does not cross the BBB. Compounds with permeability values above 0.3 are generally considered capable of penetrating the BBB. Thus, AINDPC is unlikely to cause adverse effects on the central nervous system. Additionally, it is neither a CYP2D6 enzyme inhibitor nor a substrate [25]. Based on the proportionality constant, the drug clearance rate of AINDPC is calculated to be 5.071 ml/ min/kg. Despite this, the compound shows no signs of hepatotoxicity or skin irritation, indicating a favorable safety profile for the liver and skin. AINDPC fulfills most ADMET criteria, supporting its potential as a safe chemotherapeutic agent. Furthermore, its bioavailability and structural stability were evaluated using the band energy gap derived from molecular orbital theory, reinforcing its suitability for drug development.

Table 6: ADME properties of the compound AINDPC

Entry	ABS	TPSA (A2)	n-ROTB	MW	LogP	n-OHN acceptors	n-OHNH donors	Lipinski's violations	Veber Violations	Egan Violation	S.A
				<500	<=5	<10	<5	<=1	<=1	<=1	0 <S.<10
AINDPC	High	138.18	4	336.10	1.31	9	3	0	1	1	3.77

Abbreviations: ABS: Absorption, TPSA: Topological Polar Surface Area, n-ROTB: Number of Rotatable Bonds, MW: Molecular Weight, Log P: logarithm of partition coefficient of compound between n-octanol and water, n-ONHN acceptors: Number of hydrogen bond acceptors, n-OHNH donors: Number of hydrogen bonds donors, S.A: Synthetic accessibility.

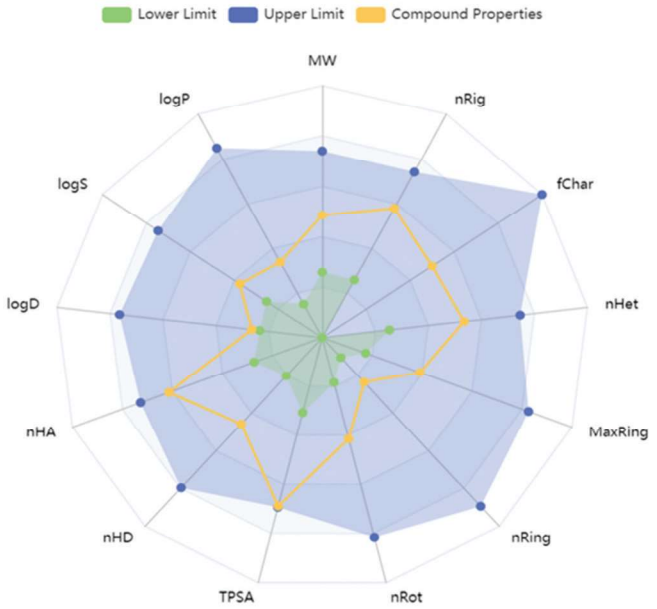

Fig. 13: Bioavailability radar for the ligand molecule of AINDPC

Table 7: Physicochemical Property of Ligand

Property	Value	Comment
Molecular Weight	336.1	Contain hydrogen atoms. Optimal:100~600
Volume	322.973	Van der Waals volume
Density	1.041	Density = MW / Volume
nHA	9	Number of hydrogen bond acceptors. Optimal:0~12
nHD	3	Number of hydrogen bond donors. Optimal:0~7
nRot	4	Number of rotatable bonds. Optimal:0~11
nRing	3	Number of rings. Optimal:0~6
MaxRing	6	Number of atoms in the biggest ring. Optimal:0~18
nHet	9	Number of heteroatoms. Optimal:1~15
fChar	0	Formal charge. Optimal:-4 ~4

nRig	20	Number of rigid bonds. Optimal:0~30
Flexibility	0.2	Flexibility = nRot /nRig
Stereo Centers	1	Optimal: 0 ~2
TPSA	138.18	Topological Polar Surface Area. Optimal:0~140
logS	-3.487	Log of the aqueous solubility. Optimal: -4~0.5 log mol/L
logP	1.315	Log of the octanol/water partition coefficient. Optimal: 0~3
logD	1.342	logP at physiological pH 7.4. Optimal: 1~3

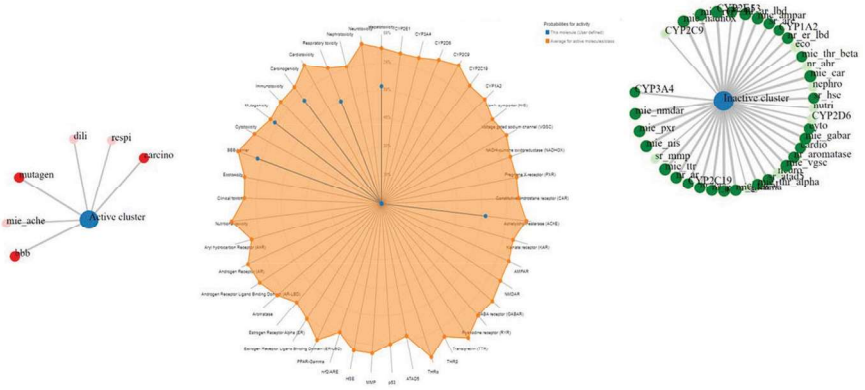

Fig. 14: Toxicity radar chart for the ligand molecule of AINDPC

6. Conclusion

The computed vibrational spectra and optimized geometric parameters aligned well with experimental observations. Using this basis set, HOMO-LUMO analysis revealed an energy gap of 1.68 eV, offering insights into the compound's reactivity, electronegativity, chemical hardness, and softness. The relatively small HOMO-LUMO gap indicates intramolecular charge transfer and reduced reactivity, suggesting high kinetic stability. The Molecular Electrostatic Potential (MEP) map highlighted electrophilic regions around the C–H bonds of the pyrazole ring and nucleophilic zones near oxygen and nitrogen atoms. ELF and Localized Orbital Locator LOL analyses confirmed the distribution of electron density, revealing reactive sites and pronounced Van der Waals interactions. Molecular docking studies showed stable binding between the compound and the 5U3A protein receptor, with a minimum binding energy of −10.09 kcal/mol, indicating strong biological interaction. Evaluations of drug-likeness and ADMET properties further demonstrated favorable pharmacokinetic and safety profiles. The title compound displays significant therapeutic promise, characterized by stable molecular behavior, well-balanced electronic properties, and encouraging biological activity. This integrated study offers a thorough understanding of its structural, electronic, and pharmacological features, supporting its

potential in pharmaceutical development. Moreover, further modification of the molecular structure and synthesis of derivatives is suggested for improving the pharmacokinetic profile and drug-like characteristics. Broader evaluation including anticancer, anti-inflammatory, and antiviral properties are also recommended for improving the therapeutic activity. To aid the preclinical phase pyrazole derivatives, adding QSAR modeling as well as ADMET and toxicity predictions are recommended for rational drug design targeting preclinical and testing phases. These modifications with pyrazole compounds will aid in further developing the base for these derivatives. While the current study highlights the antimicrobial potential of AINDPC, further investigations are required to comprehensively assess its activity. Future work will focus on determining the minimum inhibitory concentration (MIC) and minimum bactericidal concentration (MBC) values, broadening the antimicrobial screening to include additional bacterial and fungal strains, and benchmarking its efficacy against standard reference drugs. These efforts will provide a more complete understanding of the biological significance and clinical applicability of AINDPC.

Acknowledgement and Author Contributions

M. Premalatha - Data curation, software, writing original draft;

K. Anitha – Conceptualization, and Supervision, writing - review and editing;

B. Revathi – Investigation and Validation;

V. Balachandran - Supervision, writing - review and editing, Formal analysis.

B. Narayana – Resources, Visualization Methodology, funding acquisition;

A. Jayashree – Resources, investigation, Data curation, Formal analysis.

Compliance with Ethical Standards

The authors declare that this research did not involve any studies with human participants or animals performed by any of the authors.

Conflict of Interest

The authors have no relevant financial or non-financial interests to disclose.

Funding Declaration

There is no funding to declare.

References

[1] O. Ebenezer, M. Shapi, J.A. Tuszynski, A Review of the Recent Development in the Synthesis and Biological Evaluations of Pyrazole Derivatives, in: Biomedicines, 2022.

[2] A.A. Bekhit, S.N. Nasralla, E.J. El-Agroudy, N. Hamouda, A.A. El-Fattah, S.A. Bekhit, K. Amagase, T.M. Ibrahim, Investigation of the anti-inflammatory and analgesic activities of promising pyrazole derivative, European Journal of Pharmaceutical Sciences, 168 (2022) 106080.

[3] A.R.I. Morsy, S.H. Mahmoud, N.M. Abou Shama, W. Arafa, G.A. Yousef, A.A. Khalil, S.K. Ramadan, Antiviral activity of pyrazole derivatives bearing a hydroxyquinoline scaffold against SARS-CoV-2, HCoV-229E, MERS-CoV, and IBV propagation, RSC Advances, 14 (2024) 27935-27947.

[4] F.E. Bennani, L. Doudach, Y. Cherrah, Y. Ramli, K. Karrouchi, M.h. Ansar, M.E.A. Faouzi, Overview of recent developments of pyrazole derivatives as an anticancer agent in different cell line, Bioorganic Chemistry, 97 (2020) 103470.

[5] A. Cetin, I. Bildirici, A study on synthesis and antimicrobial activity of 4-acyl-pyrazoles, Journal of Saudi Chemical Society, 22 (2018) 279-296.

[6] B. Ramesh, C.M. Bhalgat, Novel dihydropyrimidines and its pyrazole derivatives: Synthesis and pharmacological screening, European Journal of Medicinal Chemistry, 46 (2011) 1882-1891.

[7] G. Ouyang, Z. Chen, X.-J. Cai, B.-A. Song, P.S. Bhadury, S. Yang, L.-H. Jin, W. Xue, D.-Y. Hu, S. Zeng, Synthesis and antiviral activity of novel pyrazole derivatives containing oxime esters group, Bioorganic & Medicinal Chemistry, 16 (2008) 9699-9707.

[8] V. Kumar, K. Kaur, D.N. Karelia, V. Beniwal, G.K. Gupta, A.K. Sharma, A.K. Gupta, Synthesis and biological evaluation of some 2-(3,5-dimethyl-1H-pyrazol-1-yl)-1-arylethanones: Antibacterial, DNA photocleavage, and anticancer activities, European Journal of Medicinal Chemistry, 81 (2014) 267-276.

[9] M.J. Frisch, G.W. Trucks, H.B. Schlegel, G.E. Scuseria, M.A. Robb, J.R. Cheeseman, G. Scalmani, V. Barone, G.A. Petersson, H. Nakatsuji, X. Li, M. Caricato, A.V. Marenich, J. Bloino, B.G. Janesko, R. Gomperts, B. Mennucci, H.P. Hratchian, J.V. Ortiz, A.F. Izmaylov, J.L. Sonnenberg, Williams, F. Ding, F. Lipparini, F. Egidi, J. Goings, B. Peng, A. Petrone, T. Henderson, D. Ranasinghe, V.G. Zakrzewski, J. Gao, N. Rega, G. Zheng, W. Liang, M. Hada, M. Ehara, K. Toyota, R. Fukuda, J. Hasegawa, M. Ishida, T. Nakajima, Y. Honda, O. Kitao, H. Nakai, T. Vreven, K. Throssell, J.A. Montgomery Jr., J.E. Peralta, F. Ogliaro, M.J. Bearpark, J.J. Heyd, E.N. Brothers, K.N. Kudin, V.N. Staroverov, T.A. Keith, R. Kobayashi, J. Normand, K. Raghavachari, A.P. Rendell, J.C. Burant, S.S. Iyengar, J. Tomasi, M. Cossi, J.M. Millam, M. Klene, C. Adamo, R. Cammi, J.W. Ochterski, R.L. Martin, K. Morokuma, O. Farkas, J.B. Foresman, D.J. Fox, Gaussian 16 Rev. C.01, in, Wallingford, CT, 2016.

[10] T. Lu, F. Chen, Multiwfn: A multifunctional wavefunction analyzer, Journal of Computational Chemistry, 33 (2012) 580-592.

[11] W. Humphrey, A. Dalke, K. Schulten, VMD: Visual molecular dynamics, Journal of Molecular Graphics, 14 (1996) 33-38.

[12] G.M. Morris, R. Huey, W. Lindstrom, M.F. Sanner, R.K. Belew, D.S. Goodsell, A.J. Olson, AutoDock4 and AutoDockTools4: Automated docking with selective receptor flexibility, Journal of Computational Chemistry, 30 (2009) 2785-2791.

[13] M. Premalatha, K. Anitha, B. Revathi, V. Balachandran, B. Narayana, A. Jayashree, N. Thirughanasambantham, Delving into 5-Amino-3-(4-chlorophenyl)-1-isonicotinoyl-2,3-dihydro-1H-pyrazole-4-carbonitrile ligand: Synthesis, spectroscopic (FT-IR, FT-Raman, NMR, UV- Vis), reactivity (ELF, LOL and Fukui), NCI, molecular docking and in silico ADMET studies by experimental and DFT methods, Journal of Molecular Structure, 1316 (2024) 138772.

[14] C. Sivakumar, B. Revathi, V. Balachandran, B. Narayana, V.V. Salian, N. Shanmugapriya, K. Vanasundari, Molecular structure, spectroscopic, quantum chemical, topological, molecular docking and antimicrobial activity of 3-(4-Chlorophenyl)-5-[4-propan-2-yl) phenyl-4, 5-dihydro-1H-pyrazol-1-yl] (pyridin-4-yl) methanone, Journal of Molecular Structure, 1224 (2021) 129286.

[15] C. Sivakumar, V. Balachandran, B. Narayana, V.V. Salian, B. Revathi, N. Shanmugapriya, K. Vanasundari, Molecular spectroscopic assembly of 3-(4-chlorophenyl)-5-[4-(propane-2-yl) phenyl] 4, 5-dihydro-1H pyrazole-1-carbothioamide, antimicrobial potential and molecular docking analysis, Journal of Molecular Structure, 1210 (2020) 128005.

[16] S. Aayisha, T.S. Renuga Devi, S. Janani, S. Muthu, M. Raja, S. Sevvanthi, DFT, molecular docking and experimental FT-IR, FT-Raman, NMR inquisitions on 4-chloro-N-(4,5-dihydro-1H-imidazol-2-yl)-6-methoxy-2-methylpyrimidin-5-amine: Alpha-2-imidazoline receptor agonist antihypertensive agent, Journal of Molecular Structure, 1186 (2019) 468-481.

[17] C. Bhaskar, N. Elangovan, S. Sowrirajan, S. Chandrasekar, O.A.A. Ali, S.F. Mahmoud, R. Thomas, Synthesis, XRD, Hirshfeld surface analysis, DFT studies, cytotoxicity and anticancer activity of di(m-chlorobenzyl) (dichloro) (4, 7-diphenyl-1,10-phenanthroline) tin (IV) complex, Journal of Molecular Structure, 1267 (2022) 133542.

[18] A. Viji, V. Balachandran, S. Babiyana, B. Narayana, V.V. Saliyan, Molecular docking and quantum chemical calculations of 4-methoxy-{2-[3-(4-chlorophenyl)-5-(4-(propane-2-yl) PHENYL)-4, 5-dihydro-1H-pyrazol-1-yl]- 1, 3-thiazol-4-yl}phenol, Journal of Molecular Structure, 1203 (2020) 127452.

[19] P.C. Jilloju, P. Shyam, A. Sanjeev, R.R. Vedula, Four-component, one-pot synthesis of (E)-N-benzylidene-3-(benzylthio)-5-(3,5-dimethyl-1H-pyrazol-1-yl)-4H-1,2,4-triazol-4-amines and their DNA binding and molecular docking studies, Journal of Molecular Structure, 1225 (2021) 129140.

[20] R. Nagalakshmi, V. Balachandran, A. Viji, B. Narayana, F. Alharethy, R. Murugan, M.K.D. Jothinathan, D. Sivasubramani, Quantum chemical calculations and molecular docking studies of 5-amino-3-(2,5-dimethoxyphenyl)-1-isonicotinoyl-2,3-dihydro-1H-pyrazole-4-carbonitrile, (2024).

[21] R. Matta, J. Pochampally, B.N. Dhoddi, S. Bhookya, S. Bitla, A.G. Akkiraju, Synthesis, antimicrobial and antioxidant activity of triazole, pyrazole containing thiazole derivatives and molecular docking studies on COVID-19, BMC Chemistry, 17 (2023) 61.

[22] A.S. Hassan, Antimicrobial evaluation, in silico ADMET prediction, molecular docking, and molecular electrostatic potential of pyrazole-isatin and pyrazole-indole hybrid molecules, Journal of the Iranian Chemical Society, 19 (2022) 3577-3589.

[23] F. En-Nahli, H. Hajji, M. Ouabane, M. Aziz Ajana, C. Sekatte, T. Lakhlifi, M. Bouachrine, ADMET profiling and molecular docking of pyrazole and pyrazolines derivatives as antimicrobial agents, Arabian Journal of Chemistry, 16 (2023) 105262.

[24] M. Rahman, J.J. Browne, J. Van Crugten, M.F. Hasan, L. Liu, B.J. Barkla, In Silico, Molecular Docking and In Vitro Antimicrobial Activity of the Major Rapeseed Seed Storage Proteins, Front Pharmacol, 11 (2020) 1340.

[25] N.H. Metwally, G.R. Saad, E.A. Abd El-Wahab, Grafting of multiwalled carbon nanotubes with pyrazole derivatives: characterization, antimicrobial activity and molecular docking study, Int J Nanomedicine, 14 (2019) 6645-6659.

[26] A.S. Hassan, N.M. Morsy, H.M. Awad, A. Ragab, Synthesis, molecular docking, and in silico ADME prediction of some fused pyrazolo[1,5-a]pyrimidine and pyrazole derivatives as potential antimicrobial agents, Journal of the Iranian Chemical Society, 19 (2022) 521-545.

[27] A. Lagunin, A. Stepanchikova, D. Filimonov, V. Poroikov, PASS: prediction of activity spectra for biologically active substances, Bioinformatics, 16 (2000) 747-748.

[28] N.C. Desai, D.V. Vaja, K.A. Jadeja, S.B. Joshi, V.M. Khedkar, Synthesis, Biological Evaluation and Molecular Docking Study of Pyrazole, Pyrazoline Clubbed Pyridine as Potential Antimicrobial Agents, Anti-Infective Agents, 18 (2020) 306-314.

[29] Y. Kaddouri, B. Bouchal, F. Abrigach, M. El Kodadi, M. Bellaoui, R. Touzani, Synthesis, Molecular Docking, MEP and SAR Analysis, ADME-Tox Predictions, and Antimicrobial Evaluation of Novel Mono- and Tetra-Alkylated Pyrazole and Triazole Ligands, Journal of Chemistry, 2021 (2021) 6663245.

[30] R. Thomas, Y.S. Mary, K.S. Resmi, B. Narayana, S.B.K. Sarojini, S. ArmakoviÄ‡, S.J. ArmakoviÄ‡, G. Vijayakumar, C.V. Alsenoy, B.J. Mohan, Synthesis and spectroscopic study of two new pyrazole derivatives with detailed computational evaluation of their reactivity and pharmaceutical potential, Journal of Molecular Structure, 1181 (2019) 599-612.

[31] N.M. Abdelazeem, W.M. Aboulthana, A.S. Hassan, A.A. Almehizia, A.M. Naglah, H.M. Alkahtani, Synthesis, in silico ADMET prediction analysis, and pharmacological evaluation of sulfonamide derivatives tethered with pyrazole or pyridine as anti-diabetic and anti-Alzheimer's agents, Saudi Pharmaceutical Journal, 32 (2024) 102025.